Sound-mediated nucleation and growth of amyloid fibrils

Anna Kozell[1‡], Aleksei Solomonov[1‡], Doron Benyamin[2], Harry Mark Greenblatt[3], Yaakov Levy[3], Irit Rosenhek-Goldian[3], Uri Raviv[2] and Ulyana Shimanovich[1]*

[1]Department of Molecular Chemistry and Materials Science, Weizmann Institute of Science, 7610001 Rehovot, Israel
[2]Institute of Chemistry, The Hebrew University of Jerusalem, Edmond J. Safra Campus, Givat Ram, Jerusalem, 9190401, Israel
[3]Department of Chemical Research Support, Weizmann Institute of Science, 7610001 Rehovot, Israel

* To whom correspondence should be addressed: ulyana.shimanovich@weizmann.ac.il

‡ These authors contributed equally.
Author Contributions: A.K. designed and performed the experiments, analyzed the data, drafted the manuscript, and prepared the figures. A.S. performed the SEM imaging, and contributed to the design of the experiments and the MD analysis. D.B. and U.R. performed the SAXS analysis and modeling. M.G. and Y.L. designed and performed the molecular dynamics simulations. I.R.-G. performed the nanoindentation measurements. U.S. devised and supervised the project, contributed to the design and implementation of the research, analysis, interpretation of the results, and the writing of the manuscript.

Keywords: amyloid, fibrillar protein self-assembly, beta-sheet conformation, ultrasound, cavitation, molecular dynamics simulations, small-angle X-ray scattering

Abstract

Mechanical energy, specifically in the form of ultrasound, can induce pressure variations and temperature fluctuations when applied to an aqueous media. These conditions can both positively and negatively affect protein complexes, influencing their stability, folding patterns, and self-assembling behavior. Regarding understanding the effects of ultrasound on the self-assembly of amyloidogenic proteins, our knowledge remains quite limited. In our recent work, we established the boundary conditions under which sound energy can either cause damage or induce only negligible changes in the structure of protein species. In the present study, we demonstrate that when the delivered ultrasonic energy is sufficiently low, it can induce refolding of specific motifs in protein monomers, as it has been revealed by MD, which is sufficient for primary nucleation, characterized by adopting a hydrogen-bonded β-sheet-rich structure. These structural changes are initiated by pressure perturbations and are accelerated by a temperature factor. Furthermore, the prolonged action of low-amplitude ultrasound enables the elongation of amyloid protein nanofibrils directly from monomeric lysozyme proteins, in a controlled manner, until they reach a critical length. Using solution X-ray scattering, we determined that nanofibrillar assemblies, formed under the influence of ultrasound energy and natively fibrillated lysozyme, share identical structural characteristics. Thus, these results contribute to our understanding of the effects of ultrasound on fibrillar protein self-assembly and lay the foundation for the potential exploitation of sound energy in a protein chemistry environment.

Introduction

Amyloid fibrils represent a group of linear protein assemblies that possess similar characteristics, such as a common structure, fibrillation pathways, and physical properties (1). These protein assemblies are associated with dual biological functionality. On the one hand, they are linked to over 60 diseases, including neurodegenerative disorders such as Alzheimer's and Parkinson's (2) , as well as lysozyme-related amyloidosis (3). On the other hand, structurally similar fibrillar assemblies were also found to play many functional roles in nature. Generally, amyloids are created through misfolding or unfolding processes of proteins under specific destabilizing conditions. Factors such as pH, ionic strength, or temperature shifts can interfere with a protein's native fold, leading to a conformational change into a hydrogen (H)-bonded β-sheet-rich structure (4). This change coincides with a protein phase transition from a soluble monomeric state to solid nanoscale fibrils. Despite extensive research on the structure, self-assembly pathways, and biophysical properties of various amyloids using various analytical techniques (5), our knowledge of how external fields impact amyloids is still limited.

External fields, particularly mechanical ones like ultrasound (US), induce various physical and chemical alterations in aqueous environments (6, 7). Such alternations can result in various effects on fibrillar protein aggregates, including aggregate disruption, acceleration of protein aggregation, changes in protein conformation, and enhancement of mass transfer. Since under the action of US three effects (mechanical, physical, and chemical) take place simultaneously, it is technologically challenging to unravel how each effect contributes separately to fibrillar protein aggregation (8, 9). Moreover, the effects of US on protein aggregation may be highly dependent on the specific protein being studied, since different proteins have varying sensitivities to mechanical stress, heat, and conformational changes induced by US. Additionally, the delivered US energy conditions, such as intensity, duration, and frequency, need to be carefully optimized to achieve the desired effect on protein aggregation.

Recently, we comprehensively studied the effect of sound energy on fibrillar protein complexes, aiming to establish boundary conditions under which sound energy causes either damage (denaturation) or conversely, can induce structural modification (10) We have established that under the action of high energy and power ultrasound (20 kHz, 7 Watts), the thermal effect is dominant for protein monomers and can lead to protein denaturation as well as reduce β-sheet content in lysozyme protein fibrils treated under these US conditions. Interestingly, short exposures of lysozyme protein species to low-amplitude (power) US did not lead to any significant structural changes; however, these exposures could still modify the chemical kinetics of protein fibrillation. Furthermore, long-time exposure of the monomeric protein to low-amplitude US enabled fibril elongation in a controlled manner. Since long-term exposure of the aqueous solution to low-amplitude US does not lead to significant thermal fluctuations (below the melting point of protein), it highlights the role of pressure in modifying the self-assembling behavior of fiber-forming proteins. To gain deeper insights into the effects of low frequency and power US on protein monomers, we performed a comprehensive structural, morphological, and molecular dynamics (MD) analysis. Using MD, we succeeded to detect the protein motifs, characterized by increased sensitivity to pressure and temperature fluctuations, which serve as a starting point for initiating structural changes and further fibrillation. Importantly, we observed that although the overall protein secondary structure is maintained, very small changes in the protein fold are sufficient to initiate protein-protein interaction and further accelerate fibril growth. Contrary to high-amplitude (power) ultrasound, where the thermal effect is dominant, at low-amplitude ultrasound, structural changes in protein species are initiated by pressure fluctuations. In summary, these results highlight the role of pressure parameters in modifying protein folding and

further contribute to our understanding of the overall effects of mechanical energy in the form of ultrasound on the protein structure and specifically on the fibrillar protein self-assembly phenomenon.

Results and discussion

Formation and growth of amyloid fibrils under low-amplitude wave US

To gain insights into the effect of US on self-assembling fibrillar lysozymes, we exposed monomeric protein to 20% amplitude of total power (2 Watts), 20 kHz for 10 min, which is equivalent to a 1000 J energy value. Surprisingly, we observed that relatively long exposures of monomeric lysozyme to low-amplitude wave US leads to the formation of fibrillar linear structures (**Fig. 1 *A*-*G***). After a short exposure time (4 min), as we previously reported (10), we revealed the presence of small particles; however, a longer exposure (10 min) of protein to low-amplitude wave US led to the formation of fibrillar assemblies 4-6 nm in width and with lengths varying between 100 and 1500 nm. Such an observation indicates that lysozyme proteins undergo nucleation and elongation under the action of these specific US conditions. The critical length for US-grown lysozyme fibrils was reached at 1000 J and with a 10 min exposure time. The growth of protein nanofibrils with US for longer than 1500 nm led to fibril fragmentation, which characterizes the typical effect of US on protein fibrils, namely, mechanical fragmentation. We hypothesized that the measured critical fibril length might originate from the correlation between the mechanical characteristics of US-formed lysozyme nanofibrils and the acting shear forces.

To confirm our hypothesis, we first performed a nanoindentation analysis of US-formed lysozyme nanofibrils in order to determine their mechanical characteristics. The results from our nanomechanical analysis, summarized in **Fig. 1 *H-J***, indicate that the measured rigidity of the US-formed nanofibrils is 13.75 GPa. Remarkably, this value is near that of fibrils formed without US exposure, which exhibited an elastic modulus of 11 GPa, as indicated in our earlier publication (10).

Morphology of amyloid fibrillar assemblies

To morphologically characterize lysozyme fibrillar assemblies formed under the action of low-amplitude wave US, atomic force microscopy (AFM) and scanning electron microscopy (SEM) analyses were carried out (**Fig. 1 *B-G***). Particles formed at 1000 J appear as short nanofibrils with dimensions of ~7 nm in height, 4-6 nm in width and lengths varying from 100 to 1500 nm. The length distribution of the obtained nanofibrils is summarized in **Fig. 1 *D*.** We observed the appearance of the fibril twist (twisted ribbon) in particles longer than 200 nm. The twist repeat along the fibril axis is left-handed, with a periodicity of ~55 nm (see **Fig. 1 *C***).

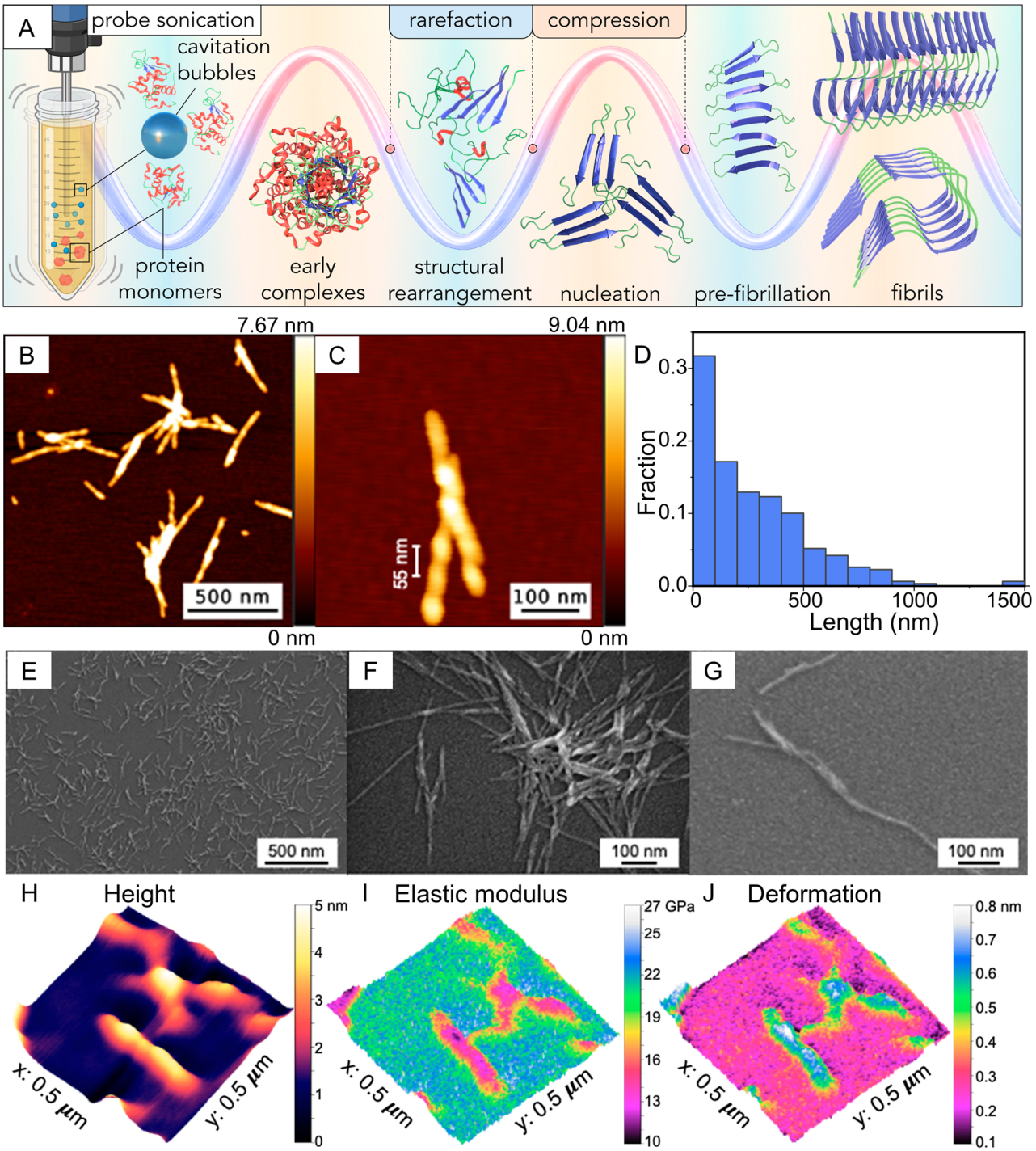

Figure 1. *(A) Schematic representation describing amyloid fibril formation and growth under the action of low-amplitude ultrasound. (B-C) Atomic force microscope (AFM) images of lysozyme aggregates and (E-G) scanning electron microscopy (SEM) images of aggregates formed by US; (D) summary of the length distribution of the formed nanofibrils. (H-J) Mechanical properties of the obtained fibrils measured by nanoindentation. Separate images were prepared with biorender.com, Blender 2.93, and Autodesk Fusion 360.*

Characterization of the structural changes imposed by sound energy on the protein monomers at low-amplitude US

Small-angle X-ray scattering (SAXS) analysis

To probe the structural organization of the US-formed nanofibrils and the existence of either structural differences or similarities between US-formed fibrils and natively aggregated lysozyme

fibrils, we performed solution small X-ray scattering analysis at the European Synchrotron Radiation Facility (ESRF) (see the Materials and methods section) (**Figure 2**). The data were analyzed using D+ software (11). Importantly, we observed that exposing natively folded lysozyme monomers to low-energy US resulted in the formation of two types of fibrillar supramolecular assemblies: wide fibrils and narrow fibrils, with mass fractions of 0.293 and 0.545, respectively **(Fig. 2 *C*)**.

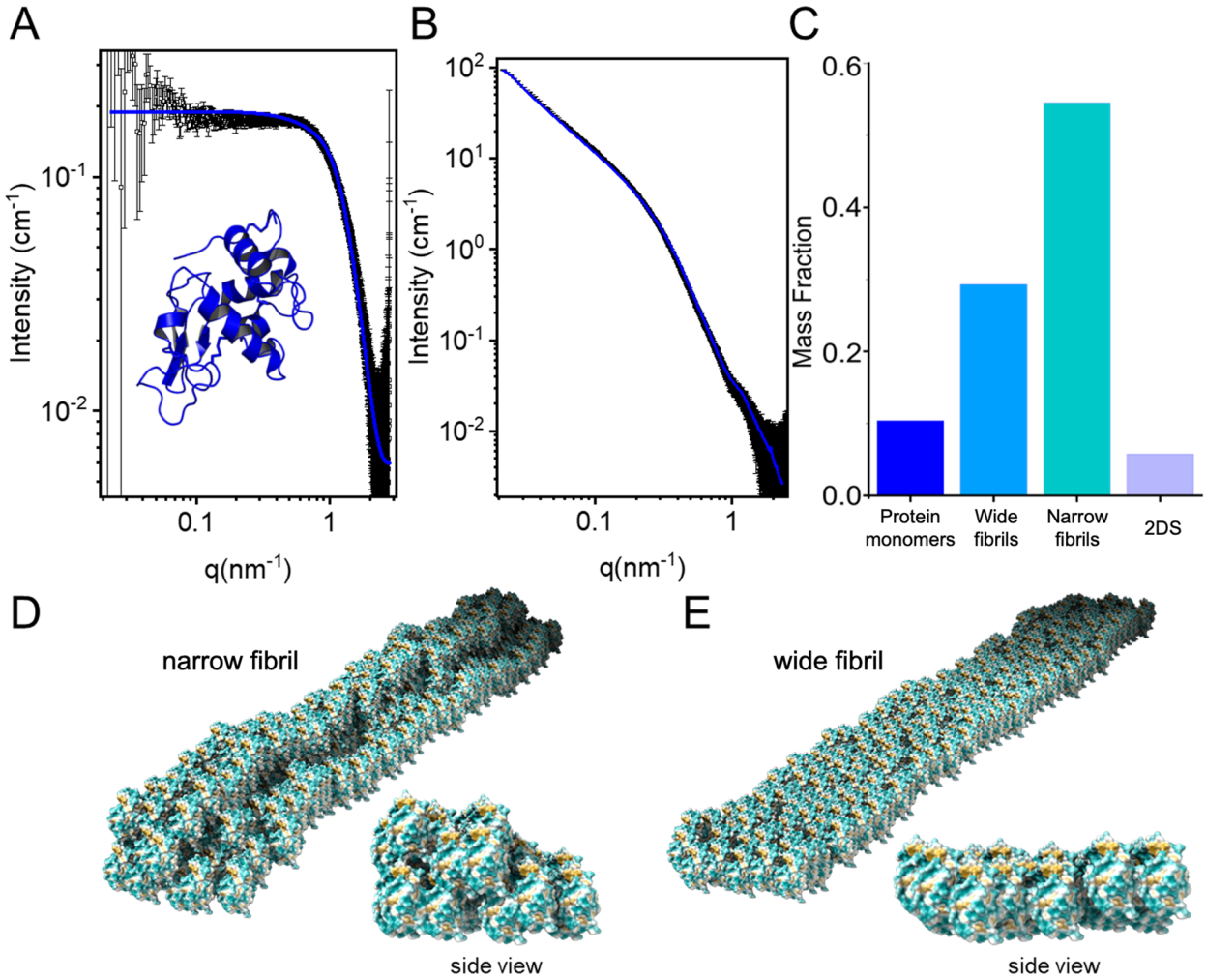

Figure 2. Small X-ray scattering analysis of azimuthally integrated background-subtracted scattering intensity I, as a function of q, the magnitude of the momentum transfer vector $\vec{q}$. *(A) Soluble monomers (reproduced from* (10) *Copyright © 2023 the Author(s). Published by PNAS), (B) Protein assemblies formed from lysozyme monomers under US irradiation and (C) corresponding mass fraction of the created species (2DS denotes 2D-sheet). Model of (D) narrow and (E) wide lysozyme fibrils formed under US based on the SAXS analysis. Fibrils visualization: ChimeraX 1.7* (12, 13).

Azimuthally integrated background-subtracted scattering intensity, I, was obtained from sonicated lysozyme monomers as a function of q, the magnitude of the momentum transfer vector $\vec{q}$ (black symbols). The model (the blue curve) was obtained by a linear combination of the monomer form-factor (M), using PDB ID:1AKI, two fibrils (wide fibrils, denoted as WF and narrow fibrils, denoted as NF), and a 2D sheet (2DS). The monomers were rotated about the z-axis by $-\frac{\pi}{9}\ rad$. We considered the contribution of thermal fluctuations, assuming a harmonic potential between the nearest-neighbor monomers, as explained (14), using a lattice elastic constant κ. From the

equipartition theorem and the value of κ, we estimated the root mean squared displacement (RMSD) of each monomer within the fibril to be $\sqrt{k_B T/\kappa}$ (10).

In a fibril of lysozyme monomers of height, H, depth, d, and width W, the location of a specific monomer, $\vec{r}_{ijk} = (x_i, y_j, z_k)$ was $x_i = iD_x$, $y_j = jD_y$, $z_k = kD_z$, where $i, j,$ and k varied between 0 and $\left\lceil \frac{W}{D_x} \right\rceil - 1$, $\left\lceil \frac{d}{D_y} \right\rceil - 1$, and $\left\lceil \frac{H}{D_z} \right\rceil - 1$, respectively. The parameters of the fibrils were $D_x = D_z = 2.6\, nm, D_y = 3.6\, nm$, $H = 400\, nm$, $w = 12\, nm$, $d = 7\, nm$, and $\kappa = 4 \pm 2 \times 10^{-20}\, J \cdot nm^{-2}$. This κ value corresponds to a RMSD value of ~0.3 nm, suggesting that the fibrils were rather soft. In the narrow fibril (NF), we deleted 2 (out of the 5) filaments of the last layer of the fibril. In the wider fibril (WF), we used the same parameters but changed the following parameters: $w = 15.6\, nm$, $d = 7.2\, nm$, and $\kappa = 6 \pm 3 \times 10^{-20}\, J \cdot nm^{-2}$ (RMSD = 0.26 nm), and we deleted the last layer of the fibril (WF). In the 2D sheet (2DS): $H = 400\, nm$, $w = 300\, nm$, $d = 6\, nm$, and $\kappa = 4 \pm 2 \times 10^{-20}\, J \cdot nm^{-2}$ (RMSD ~ 0.3 nm).

Thus, our analysis revealed that low-amplitude wave US triggered the formation of two types of nanofibrils: narrow (**Fig. 2 *D***) and wide (**Fig. 2 *E***).

Secondary structure evaluation using Fourier transform infrared spectroscopy (FTIR) analysis of aggregated protein nanofibrils.

To establish the structural arrangements of fibrils that resulted from exposing lysozyme monomers to ultrasound (US), we conducted a secondary structure analysis by using Fourier-transform infrared spectroscopy (FTIR). In particular, we focused on the alterations in the vibration bands associated with amide I and amide II. This enabled us to detect the structural changes imposed by the action of US.

The experiment was performed in a deuterated solvent. Traditionally, studying the protein secondary structure, using deuterated solvents, such as deuterated water (D_2O), is a common practice in FTIR spectroscopy. Standard water can interfere with the measurements due to the strong absorption bands of its O-H stretching vibrations, which overlap with the proteins' amide I and amide II bands. However, deuterated solvents help to minimize such interference and improve the quality of the acquired spectra. D_2O exhibits a lower absorption in the region of interest for protein secondary structure analysis, since the O-D stretching vibrations occur at different wavenumbers compared with the O-H stretching. This allows for a clearer observation of the amide I and amide II bands (**Fig. 3 *A***), which are crucial for evaluating the protein secondary structure. The aggregated amyloid structures' vibration spectra are characterized by intermolecular β-sheet content (1610-1625 cm^{-1}) and antiparallel amyloid β-sheets (1690-1705 cm^{-1}) (15). These spectra, which differ from the characteristic vibrations of the native protein fold, are 1625-1635 cm^{-1} for β-sheet content, 1635-1665 cm^{-1} for α-helix and random coils, and 1665-1690 cm^{-1} for β-turns (**Fig. 3 *C-E***).

We found that the secondary structure of the monomeric lysozyme undergoes significant changes when exposed to low-amplitude ultrasound for 10 minutes. The content of β-sheet significantly increases, adopting a conformation typical for amyloids (summarized in **Fig. 3 *B***).

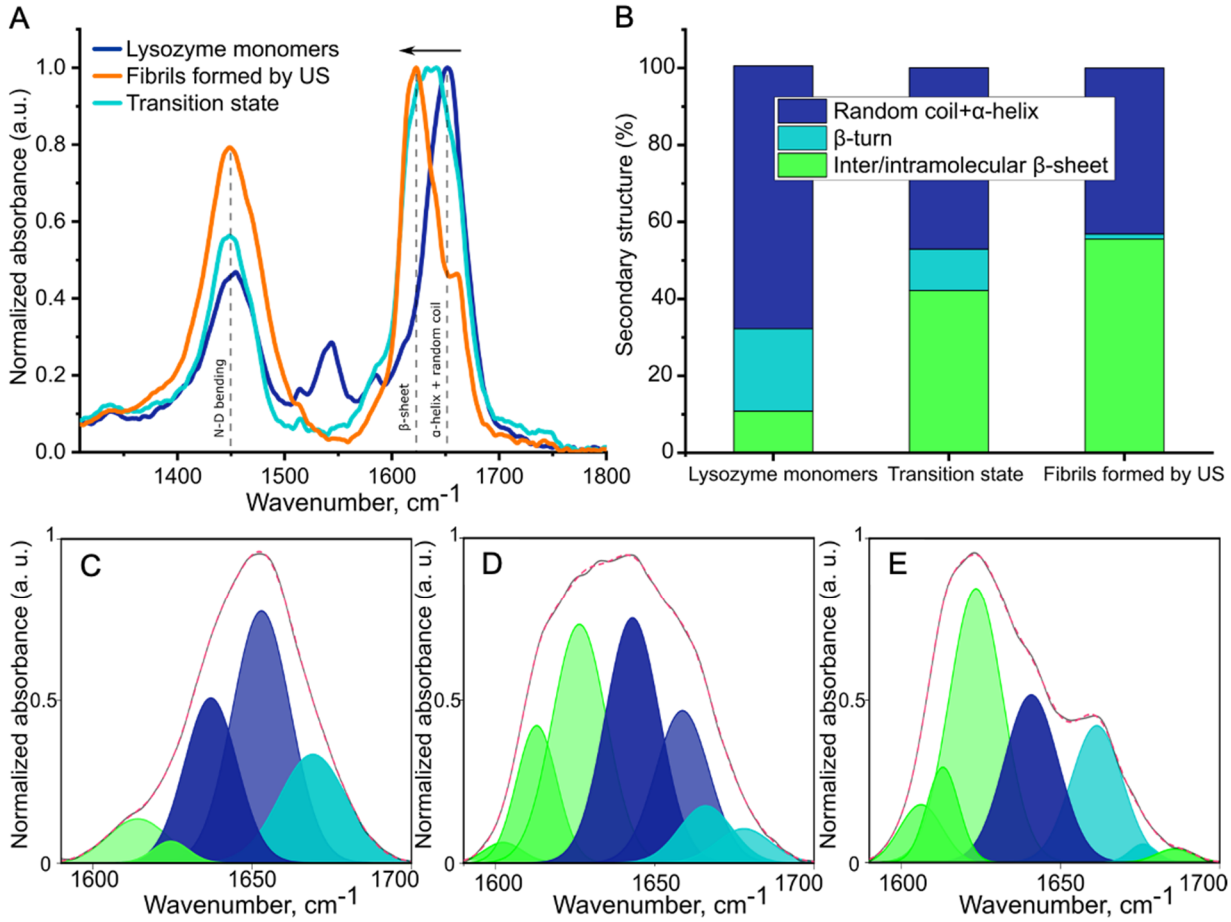

Figure 3. FTIR analysis of lysozyme monomers and nanofibrils formed due to low-amplitude US. *(A) Amide I and Amide II bands of the FTIR spectra of lysozyme monomers (blue), transition state – a nanofibril solution after 8 min of US (cyan), and a nanofibril solution after 10 min of US (orange). (B) A comparative analysis of the secondary structure in %. (C) Deconvoluted Amide I band of lysozyme monomers, (D) transition state of a nanofibril solution, and (E) final nanofibril solution.*

Molecular dynamics simulations

To gain further insight into the mechanism underlying lysozyme fibrillation under low-amplitude ultrasound, we performed molecular dynamics (MD) simulations. The main physical factors that are created during ultrasound treatment and that have an impact on the medium and protein are temperature and pressure. When operating in low-frequency ultrasonic mode (20 kHz), cavitation bubbles form and collapse, which also leads to significant effects associated with the formation of acoustic flows, leading to an increase in the speed of the movement of molecules in the medium. Local point changes in pressure and temperature in this mode can reach 1,000 bar and 5,000 K (16–19), respectively, coupled with the formation of local cavitation voids with low pressure. We further focused on examining how these factors affect the structural integrity of the protein. To this end, we carried out computer modeling of the behavior of lysozyme monomers, using conditions (pressure and temperature) like those that appear during the treatment of protein solutions with ultrasound; we monitored changes both in the complete structure of the protein and in all of its individual secondary structure elements (*α*-helixes, *β*-sheets, and several random coils). The lysozyme protein (hen egg white lysozyme, HEWL, PDB: 193L, **Fig. 4** ***A***), was chosen for simulations consisting of 129 amino acid residues and 8 *α*-helixes (H) and 2 *β*-sheets (S): H1 (α-helix, 5-14, RCELAAAMKR), H2 (*α*-helix, 20-22, YRG), H3 (*α*-helix, 25-36, LGNWVCAAKFES), S1 (*β*-sheet, 43-45, TNR), S2 (*β*-sheet,

51-53, TDY), H4 (α-helix, 80-84, CSALL), H5 (*α*-helix, 89-99, TASVNCAKKIV), H6 (*α*-helix, 104-107, GMNA), H7 (*α*-helix, 109-114, VAWRNR), H8 (*α*-helix, 120-124, VQAWI).

We carried out three different simulation routes (two runs for each) for 3 microseconds in 1 picosecond increments ($3 \cdot 10^6$ points) for three states of the protein in aqueous solutions: at 300 K (the initial conditions after solvation), then at an elevated temperature of 338 K (65 °C), and at 338 K 25 bar pressure and took snapshots at different times for each simulation (**Fig. 4 *B***). The 338 K thermal condition was chosen as the starting point for three different reasons. First, 338 K is the measured temperature that appears upon exposing aqueous protein solution to sound energy with an amplitude of 2 watts (20% power). Second, not related to the sonication condition, traditionally amyloidogenic fibrillation is initiated and accelerated when protein species are exposed to 338 K (10, 20–22). Third, lysozyme is a relatively stable protein, having rather high melting point at different conditions varying from 69 °C to 74 °C in the pH range of 3–7.4 (23, 24). Former MD simulations confirmed that rather high temperature required (370 K) to initiate and keep the unfolding process of lysozyme (25). Thus, we hypothesized that at 338 K the initial stages of structural changes, namely, structural reorganization, might take place. To test our hypothesis, the 25-bar condition was chosen, based on the following assumptions: Although the local change in pressure can be significant, the effective pressure, like the temperature of the solution, is a global quantity that determines the behavior of molecules. The effective pressure was estimated from the acoustic power type (ca. 2 $W \cdot mm^{-2}$) and the acoustic impedance of the aqueous solutions (26–28). Considering the density of water at 20-65 °C, the speed of sound in water under the same conditions, as well as its density (whose product gives the acoustic impedance), it can be estimated that the effective pressure lies in the range of 2.4-2.5 MPa (and, of course it increases when the acoustic intensity or the sonication power increases). Considering the presence of the protein in solution, as well as the deviations in ultrasound power, we can conditionally assume an effective pressure of 25 bar. However, it must be understood that this pressure value is approximate, since the treatment of protein solutions with ultrasound is a non-equilibrium process and the effective pressure can be higher and vary within a wider range. However, this pressure value serves as a good starting point for more complex calculations that can be carried out in more detail later.

At elevated temperature and pressure, after a certain period of structure stabilization, an increase in the RMSD may occur over time and, apparently, may have cumulative and synergistic effects.

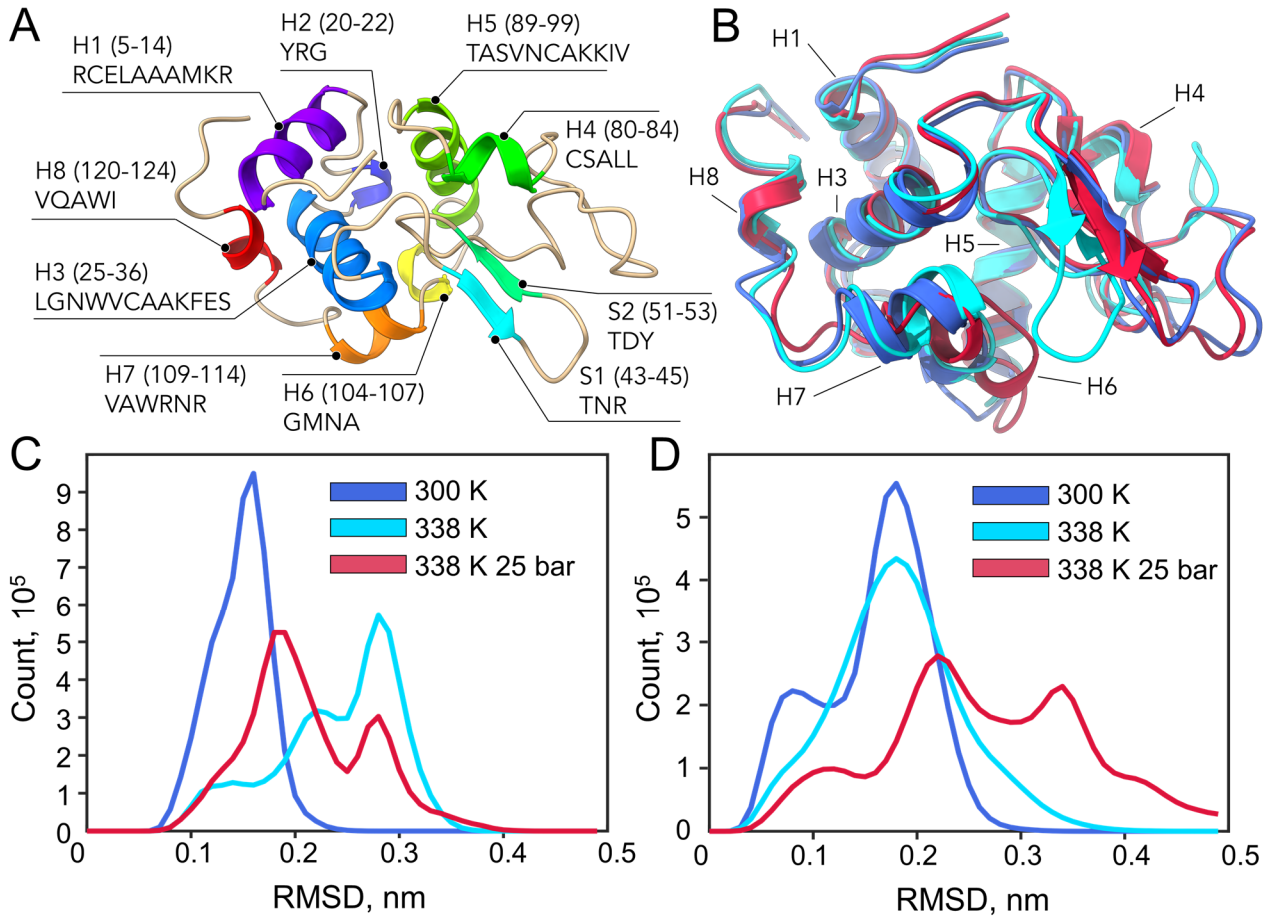

Figure 4. *(A) Chemical structure of hen egg white lysozyme (HEWL, PDB: 193L, 129 amino acid residues) represented as a cartoon model. The α-helix and β-sheet structures are shown in rainbow colors and are denoted by the letters "H" and "S", correspondingly, next to their positions in the protein structure and the amino acid sequence. Numeration of elements started from the N-terminal; (B) the superposition of three protein structures under different conditions and different simulation time frame snapshots: blue – at 300 K, cyan – at 338 K (t = 449693 ps), and red – at 338 K 25 bar (t = 1843799 ps), pointing to key structural elements; visualization: ChimeraX 1.7; diagrams of cumulative (0 – 3000000 ps) RMSD of C_α over two runs for (C) the whole protein sequence and (D) for H7 (see* **Fig. 4** ***A****) under different simulation conditions (referred to SI Appendix,* **Fig. S2** *and* **Fig. S11***, correspondingly).*

One of the main indicators of the structural stability of proteins during MD simulations is the dependence of the root mean square deviation (RMSD) of C_α (*SI Appendix,* **Fig. S1**) over time, whose change was manifested by the mobility of the protein backbone, as well as the stability of the tertiary structure itself. Over two runs in an aqueous solution at 300 K, lysozymes had an average C_α RMSD value of approximately 0.152 ± 0.027 nm with a maximum at 0.285 nm. At 338 K, the mean RMSD equals 0.245 ± 0.059 nm with a maximum of 0.408 nm. At 338 K and 25 bar, the mean RMSD was 0.217 ± 0.059 nm with a maximum of 0.445 nm (see **Table 1**).

From the analysis, presented in *SI Appendix,* **Fig. S2**, the RMSD value of C_α increases with an increase in either temperature or pressure, confirming the occurrence of protein fold destabilization. At room temperature (RT), namely, at 300 K, our RMSD analysis confirmed that the protein structure is stable (see *SI Appendix,* **Fig. S2**). During the MD simulations, the temperature was increased to 338 K; consequently, the RMSD increased to ca. 0.3 nm over a period of approximately 500-750 ns, indicative of partial destabilization of the protein fold. Interestingly, the exposure of protein

monomers to pressure (25 bar, which is equivalent to pressure conditions created by ultrasound in aqueous media), overall stabilizes the protein fold, observed from cumulative RMSD analysis (*SI Appendix,* **Fig. S13** and **Fig. S14** ***A***). The combined action of elevated temperature (to 338 K) and pressure (25 bar) enabled us to perform a detailed analysis of the protein fragments and to track the conformational changes in these fragments. The exact sequences of the fragments, which have been presented earlier (also see **Fig. 4** ***A***), are summarized in **Table 1**.

Table 1. *Mean, median and maximum RMSD value (nm) for C_α under different conditions over 2 runs during 3 µs (with a step of 1 ps) for full protein chains and for each structural element of its secondary structure (referred to in* **Fig. 4** ***A****). A graphical representation of the RMSD summary is presented in SI Appendix,* **Fig. S13**.

Structure	300 K			338 K			338 K 25 bar		
	Mean	**Median**	**Max**	**Mean**	**Median**	**Max**	**Mean**	**Median**	**Max**
Entire protein chain	0.152 ± 0.027	0.155	0.285	0.245 ± 0.059	0.258	0.408	0.217 ± 0.059	0.206	0.445
H1 RCELAAAMKR	0.092 ± 0.038	0.083	0.306	0.110 ± 0.049	0.098	0.373	0.108 ± 0.046	0.096	0.486
H2 YRG	0.101 ± 0.046	0.092	0.441	0.128 ± 0.064	0.115	0.652	0.148 ± 0.095	0.123	0.878
H3 LGNWVCAAKFES	0.101 ± 0.033	0.104	0.232	0.116 ± 0.035	0.121	0.270	0.132 ±0.026	0.130	0.300
S1 TNR	0.116 ± 0.054	0.103	0.374	0.190 ± 0.063	0.190	0.470	0.166 ± 0.062	0.162	0.450
S2 TDY	0.088 ± 0.029	0.086	0.294	0.131 ± 0.046	0.135	0.337	0.107 ± 0.041	0.103	0.314
H4 CSALL	0.080 ± 0.031	0.074	0.309	0.144 ± 0.047	0.148	0.391	0.098 ± 0.035	0.092	0.379
H5 TASVNCAKKIV	0.093 ± 0.029	0.089	0.250	0.117 ± 0.040	0.112	0.453	0.102 ± 0.031	0.098	0.366
H6 GMNA	0.247 ± 0.137	0.233	0.691	0.345 ± 0.172	0.356	0.995	0.508 ± 0.260	0.504	1.23
H7 VAWRNR	0.164 ± 0.052	0.173	0.398	0.187 ± 0.061	0.186	0.538	0.277 ± 0.106	0.268	0.714
H8 VQAWI	0.088 ± 0.026	0.085	0.325	0.112 ± 0.050	0.099	0.548	0.163 ± 0.113	0.121	0.869

During this period, compared to high temperature alone, high pressure can slightly stabilize the molecule (**Fig. 4** ***C***); however, its effect on individual structural elements may be greater than on the other elements and the full protein chain **Fig. 4** ***D***. But overall, the simulations carried out revealed changes in all structural elements in proteins both at elevated temperatures alone and after applying additional pressure; over time, pressure indeed destabilizes the structure compared with non-elevated temperature conditions (see *SI Appendix,* **Fig. S13**).

According to the mean RMSD value, temperature and pressure have a minimal impact on helix H1, H2, and H3 (see **Table 1** and *SI Appendix,* **Fig. S3-S5**, **S13**, **S14**), where C_α in H1 did not show any significant changes over time (see *SI Appendix,* **Fig. S3**, **S4**).

For S1, S2, H4, and H5, we observed that pressure stabilizes the structure of the fragments, which is opposite to the effect of elevated temperature alone (see **Table 1** and *SI Appendix,* **Fig. S6-S9**, **S13**, **S14**). However, the effect is rather minor, with no appreciable trend observed for the RMSD of C_α. Nevertheless, the overall structure becomes less stable than the fold of the above-mentioned

fragments at 300 K.

For fragments H6-H8 (**Fig. 4 *D*,** see also **Table 1** and *SI Appendix,* **Fig. S13**, **S14**), pressure had a significant destabilization effect on the fragment fold, which is reflected in increased values of mean RMSD. When the temperature and pressure factors were combined, the fold-modifying effect becomes even more pronounced, altering the fragment fold integrity. The dependence on the RMSD of C_α displays a sustainable increasing trend according to the time under high pressure (*SI Appendix,* **Fig. S10-S12**), particularly for H6 and H7. The H6 fragment was found to be highly sensitive specifically to thermal fluctuations. Thus, even at temperatures slightly above the RT, variations in RMSD were observed, which became more pronounced over time. H8 also undergoes destabilization with increased temperature and pressure, but it is less variable than H6 and H7. Although the conformation of H6-H8 changes, it is important to note that they do not fully unfold/refold during the 3 μs MD simulations.

Thus, overall, even though lysozyme at 338 K does not undergo significant changes in protein folding under increased pressure, the combined effect of pressure and temperature factors can serve as a trigger to destabilize the individual structural fragments. The fragments of H6–H8 were identified by us, using MD, as structurally sensitive motifs, which are more prone to restructuring than the others. Thus, under elevated temperature and pressure conditions, fragments undergo partial protein unfolding and adapt a new aggregative β-sheet conformation, an essential early step in amyloidogenic protein fibrillation.

Conclusions

Our investigation into the effect of ultrasound on the self-assembly of amyloidogenic proteins has yielded significant insights. Our findings indicate that mechanical energy, when applied to aqueous media, can lead to pressure and temperature variations, both enhancing and compromising protein complexes' stability, folding, and self-assembling patterns. Prolonged exposure to low-amplitude ultrasound allows for the controlled elongation of amyloid protein nanofibrils from monomeric lysozyme protein until they attain a critical length. Low ultrasonic energy levels induce refolding of certain protein motifs. Molecular dynamics revealed that this refolding might give rise to primary nucleation driven by pressure changes and that it is further amplified by temperature variations. Solution X-ray scattering data and secondary structure evaluation by FTIR spectroscopy confirmed that the nanofibrillar assemblies created through ultrasound energy and natively fibrillated lysozymes are structurally similar. In essence, our findings enhance our understanding of ultrasound's role in fibrillar protein self-assembly and highlight its potential applicability in protein chemistry.

Acknowledgments

U.S. acknowledges financial support from the Gruber Foundation, the Nella and Leon Benoziyo Center for Neurological Diseases. In addition, U.S. thanks the Perlman family for funding the Shimanovich Lab at the Weizmann Institute of Science: “This research was made possible in part by the generosity of the Harold Perlman Family.” The authors would like to acknowledge partial support from the GMJ Schmidt Minerva Center of Supramolecular Architectures at the Weizmann Institute, the Mondry Family Fund for the University of Michigan/Weizmann collaboration, the Gerald Schwartz and Heather Reisman Foundation, and the WIS Sustainability and Energy Research Initiative (SAERI). This research was supported by a research grant from the Tom and Mary Beck Center for Advanced and Intelligent Materials at the Weizmann Institute of Science, Rehovot, Israel. Molecular graphics and analyses were performed with UCSF ChimeraX, developed by the Resource for Biocomputing, Visualization, and Informatics at the University of California, San Francisco, with

support from National Institutes of Health R01-GM129325 and the Office of Cyber Infrastructure and Computational Biology, National Institute of Allergy and Infectious Diseases. The authors are also grateful to Steve Manch for the English editing.

Materials and Methods

Preparation of lysozyme monomer solution

Monomer solution: Lyophilized egg white lysozyme (Sigma-Aldrich) was dissolved in 20 mM NaCl + 10 mM HCl at 20 $mg \cdot ml^{-1}$ (1.4 mM).

Ultrasound treatment of lysozyme monomers

Lysozyme monomer solutions were subjected to sonication using an Ultrasonic Processor (QSONICA) operating at 20 kHz. The sonication was carried out at 20% amplitude (2 W of delivered power).

Morphological analysis by Atomic Force Microscopy (AFM)

Sample preparation: a small droplet (50 µl) of a fibril/monomer suspension was deposited onto freshly cleaved mica, allowed to stand for 2 min, washed several times with distilled water, and then dried. AFM tapping-mode measurements were carried out using AC240 cantilevers on a NanoWizard 4 instrument in an acoustic enclosure (JPK Instruments). JPK Data Processing Software was used for image analysis and ImageJ software for statistical data collection.

Field Emission High Resolution Scanning Electron Microscopy (FE-HRSEM)

FE-HRSEM images were obtained using Ultra-55 Ultra-high-resolution SEM (Carl Zeiss, Germany) with an accelerating voltage of 2-3 kV for both In-Lens and Everhart-Thorney secondary electron (SE2) detectors under a vacuum of $<2 \cdot 10^{-5}$ mbar with a working distance of 2.4-4 mm and an aperture of 30 µm. For imaging, a drop of liquid samples of lysozyme fibrils was spread onto a 2 × 2 cm^2 mica sheet attached to a 20 × 75 mm^2 microscope glass for 2 min, gently rinsed with Milli-Q triple distilled water, and dried under a gentle nitrogen stream (like sample preparation in the "Morphological analysis by AFM" section). Before imaging, the slides were attached to aluminum stubs with carbon tape (2SPI, USA), and partially coated with carbon paste (2SPI, USA); finally, 2–3 nm of Iridium was sputtered on the samples using a CCU-010 HV high-vacuum ($8 \cdot 10^{-3}$ – $5 \cdot 10^{-5}$ mbar) sputter coater (Safematic, Switzerland) at a rate of 0.01–0.05 $Å \cdot s^{-1}$ to improve the image contrast, sample conductivity, and stability during imaging.

AFM nanomechanical measurements

Imaging and mechanical properties were measured using PeakForce QNM on a Multimode AFM (Bruker). AC160 (Olympus) with a spring constant of 40 N/m probes was used. For the former, the effective tip radius was calibrated on a sample of HOPG with a modulus of 18 Gpa Deformation depths that were kept to about 1 nm. The Bruker software (Nanoscope 9.2) was used to compute the elastic modulus maps using the DMT model to fit the force vs. the deformation curves. Gwyddion open-source software was used for the image analysis. All averaged modulus values were calculated from the center of each fibril or aggregate.

Small-angle X-ray scattering (SAXS) measurements

All solution SAXS measurements were measured at ID02 beamline at the European Synchrotron Radiation Facility (ESRF). The analysis was performed using a beam size of $32.4 \times 145\ \mu m^2$

(vertical and horizontal, respectively), a photon energy of 12.23 keV, an Eiger2 4M (Dectris AG) detector, a sample-to-detector distance of 3.114 m, and an exposure time of 0.1 s.

SAXS Models

All the models were computed after translating their center of mass to the origin. We assumed an instrument Gaussian resolution function with a standard deviation of 0.001, as explained. Other D+ computational parameters were as follows: an Integration Method: Monte Carlo (Mersenne Twister), Integration iterations: 10^6, Monomer Grid Size: 20, the Number of Generated Points: 300, Convergence: 0.001, and the Update interval: 500 ms. The hydration layer was computed assuming an outer solvent electron density of $340\ e \cdot mm^{-3}$, using the dummy atoms method, a solvation thickness of 0.28 nm, a solvation probe radius of 0.14 nm, a solvent voxel size of 0.2 nm, $C_1 = 1$, and a solvent electron density of $333\ e \cdot mm^{-3}$. We used the Hybrid method with a reciprocal grid for the monomer. These parameters are explained in our earlier publication (11).

The atomic model of the fibrils was created by docking copies of the atomic model of the hydrated lysozyme monomer into the fibril assembly symmetry (describing the rotations and translations of each monomer subunit). In a fibril of height H, depth d, and width W, the location of a specific monomer, $\vec{r}_{ijk} = (x_i, y_j, z_k)$, is $x_i = iD_x, y_j = jD_y$, $z_k = kD_z$, where $i, j,$ and k vary between 0 and $\left\lceil\frac{W}{D_x}\right\rceil - 1$, $\left\lceil\frac{d}{D_y}\right\rceil - 1$, and $\left\lceil\frac{H}{D_z}\right\rceil - 1$, respectively. H, W, and d vary between different fibril models. The spacing between the centers of adjacent monomers in the $x, y,$ and z directions, where $D_x = D_y = D_z$is $3.0 \pm 0.1\ nm$ in all the models. The orientation of the monomer was the same in all the samples, given by $\alpha_{ijk} = \beta_{ijk} = \gamma_{ijk} = 0$, using the Tait-Brain notation. We considered the contribution of thermal fluctuations, assuming a harmonic potential between the nearest-neighbor monomers, as explained in our earlier publication.

After introducing thermal fluctuations in all the fibril models, we deleted half of the last layer by removing monomers with indexes $\left\lceil\frac{W}{2D_x}\right\rceil < i < \left\lceil\frac{W}{D_x}\right\rceil$, $j = \left\lceil\frac{d}{D_y}\right\rceil - 1$, and $0 \leq k < \left\lceil\frac{H}{D_z}\right\rceil$. To all the models, a very small constant background factor was added to optimize the fit.

Protein secondary structure elucidation using FTIR spectroscopy

The measurements were performed in deuterated solvent (D_2O). Structural analysis of the lysozyme fibrils and monomers was performed using an FTIR spectrometer, Nicolet iS50, with an Attenuated Total Reflection (ATR) accessory (Thermo Scientific). The samples were used without further pretreatment, loaded into the ATR holder, and analyzed by subtracting a water reference. The atmospheric compensation spectrum was subtracted from the original FTIR spectra, and a second derivative was applied for further analysis. OMNIC spectroscopy software (Thermo Scientific) and OriginLab software were used to resolve the spectra.

Molecular dynamics simulations

The starting model for hen egg white lysozyme (HEWL) was taken from the PDB databank (PDB: 193L). Before simulations, all water in the model was removed; however, the bound sodium and chloride ions were preserved. To somewhat simulate the experimental conditions of pH 2.0, all histidines and carboxylic acid groups were protonated. Gromacs 2022.1 was used with the Amber99SB-ILDN force field and the SPCE water model. The salt concentration was set to 20 mM (NaCl) and somewhat adjusted to neutralize the charge of the system. Following minimization of the solvated system and equilibration with the NVT regime, three separate NPT regimes were carried out

for each of the three conditions: the room temperature with ambient pressure (300 K), high temperature (338 K) with ambient pressure, and high temperature with high pressure (338 K, 25 bar). This was followed by two production runs under each condition, for 3,000 ns for each run. The molecule was solvated in a water dodecahedron box. Temperature was controlled via a Berendsen temperature coupling thermostat, whereas the pressure was controlled via a Parrinello-Rahman pressure coupling barostat. Extraction of the data from the time-dependent RMSD and transforming them into the cumulation diagrams presented in *SI Appendix,* **Fig. S2-S12** were performed using Matlab scripts. Structural alignment for presentations and analysis was done in ChimeraX 1.7 using "matchmaker" command (see **Fig. 4 *B***).

References

1. T. P. J. Knowles, M. J. Buehler, Nanomechanics of functional and pathological amyloid materials. *Nat. Nanotechnol.* **6**, 469–479 (2011).
2. F. Chiti, C. M. Dobson, Protein misfolding, amyloid formation, and human disease: A summary of progress over the last decade. *Annu. Rev. Biochem.* **86**, 27–68 (2017).
3. M. B. Pepys, *et al.*, Human lysozyme gene mutations cause hereditary systemic amyloidosis. *Nature* **362**, 553–557 (1993).
4. L. Nielsen, *et al.*, Effect of environmental factors on the kinetics of insulin fibril formation: Elucidation of the molecular mechanism. *Biochemistry* **40**, 6036–6046 (2001).
5. T. P. J. Knowles, *et al.*, An analytical solution to the kinetics of breakable filament assembly. *Science (80-.).* **326**, 1533–1537 (2009).
6. A. Weissler, I. Pecht, M. Anbar, Ultrasound chemical effects on pure organic liquids. *Science (80-.).* **150**, 1288–1289 (1965).
7. C. L. Hawkins, M. J. Davies, Generation and propagation of radical reactions on proteins. *Biochim. Biophys. Acta - Bioenerg.* **1504**, 196–219 (2001).
8. U. Shimanovich, G. J. L. Bernardes, T. P. J. Knowles, A. Cavaco-Paulo, Protein micro- and nano-capsules for biomedical applications. *Chem. Soc. Rev.* **43**, 1361–1371 (2014).
9. O. Grinberg, U. Shimanovich, A. Gedanken, Encapsulating bioactive materials in sonochemically produced micro- and nano-spheres. *J. Mater. Chem. B* **1**, 595–605 (2013).
10. A. Kozell, *et al.*, Modulating amyloids' formation path with sound energy. *Proc. Natl. Acad. Sci. U. S. A.* **120**, e2212849120 (2023).
11. A. Ginsburg, *et al.*, D+: software for high-resolution hierarchical modeling of solution X-ray scattering from complex structures. *J. Appl. Crystallogr.* **52**, 219–242 (2019).
12. T. D. Goddard, *et al.*, UCSF ChimeraX: Meeting modern challenges in visualization and analysis. *Protein Sci.* **27**, 14–25 (2018).
13. E. F. Pettersen, *et al.*, UCSF ChimeraX: Structure visualization for researchers, educators, and developers. *Protein Sci.* **30**, 70–82 (2021).
14. D. Louzon, *et al.*, Structure and Intermolecular Interactions between L-Type Straight Flagellar Filaments. *Biophys. J.* **112**, 2184–2195 (2017).
15. L. W. Y. Roode, U. Shimanovich, S. Wu, S. Perrett, T. P. J. Knowles, Protein Microgels from Amyloid Fibril Networks. *Adv. Exp. Med. Biol.* **1174**, 223–263 (2019).
16. K. S. Suslick, Sonochemistry. *Science (80-.).* **247**, 1439–1445 (1990).
17. E. B. Flint, K. S. Suslick, The temperature of cavitation. *Science (80-.).* **253**, 1397–1399 (1991).
18. A. V. Pandit, V. P. Sarvothaman, V. V. Ranade, Estimation of chemical and physical effects of cavitation by analysis of cavitating single bubble dynamics. *Ultrason. Sonochem.* **77**, 105677. (2021).
19. Y. G. Adewuyi, Sonochemistry: Environmental science and engineering applications. *Ind. Eng. Chem. Res.* **40**, 4681–4715 (2001).
20. M. Xu, *et al.*, The first step of hen egg white lysozyme fibrillation, irreversible partial unfolding, is a two-state transition. *Protein Sci.* **16**, 815–832 (2007).

21. X. M. Zhou, *et al.*, Enzymatically Active Microgels from Self-Assembling Protein Nanofibrils for Microflow Chemistry. *ACS Nano* **9**, 5772–5781 (2015).
22. U. Shimanovich, *et al.*, Protein microgels from amyloid fibril networks. *ACS Nano* **9**, 43–51 (2015).
23. S. Venkataramani, J. Truntzer, D. R. Coleman, Thermal stability of high concentration lysozyme across varying pH: A Fourier Transform Infrared study. *J. Pharm. Bioallied Sci.* **5**, 148–153 (2013).
24. C. O. Silva, *et al.*, Lysozyme photochemistry as a function of temperature. the protective effect of nanoparticles on lysozyme photostability. *PLoS One* **10,** e0144454 (2015).
25. M. Jafari, F. Mehrnejad, Molecular insight into human lysozyme and its ability to form amyloid fibrils in high concentrations of sodium dodecyl sulfate: A view from molecular dynamics simulations. *PLoS One* **11**, e0165213 (2016).
26. B. Sorum, R. A. Rietmeijer, K. Gopakumar, H. Adesnik, S. G. Brohawn, Ultrasound activates mechanosensitive TRAAK K+ channels through the lipid membrane. *Proc. Natl. Acad. Sci. U. S. A.* **118**, e2006980118 (2021).
27. R. Hatakeyama, M. Yoshizawa, T. Moriya, Method for the measurement of acoustic impedance and speed of sound in a small region of bone using a fused quartz rod as a transmission line. *Japanese J. Appl. Physics, Part 1 Regul. Pap. Short Notes Rev. Pap.* **39**, 6449–6454 (2000).
28. R. Alkins, K. Hynynen, Ultrasound Therapy. *Compr. Biomed. Phys.* **10**, 153–168 (2014).